CrossMark

Systematic Design of Optimal Low-Thrust Transfers for the Three-Body Problem

Shankar Kulumani[1] (ORCID) · **Taeyoung Lee[1]**

Abstract

We develop a computational approach for the design of continuous low thrust transfers in the planar circular restricted three-body problem. The use of low thrust propulsion allows the spacecraft to depart from the natural dynamics and enables a wider range of transfers. We generate the reachable set of the spacecraft and use this to determine transfer opportunities, analogous to the intersection of control-free invariant manifolds. The reachable set is developed on a lower dimensional Poincaré section and used to design transfer trajectories. This is solved numerically as a discrete optimal control problem using a variational integrator, which preserves the geometric structure of the motion in the three-body problem. We demonstrate our approach with two numerical simulations of transfers in the Earth-Moon three-body system.

Introduction

Designing spacecraft trajectories is a classic and ongoing topic of research. There has been significant research into the design of orbital transfers for space vehicles. Optimal expenditure of onboard propellant is critical to allowing a mission to continue for a longer period of time or to enable the launch of a less massive spacecraft. Electric propulsion systems offer a much greater specific impulse than chemical systems. As a result, the greatly increased efficiency allows for greater payload mass or extended duration missions. However, these electric propulsion systems typically have much

---

✉ Shankar Kulumani
skulumani@gwu.edu

Taeyoung Lee
tylee@gwu.edu

[1] Department of Mechanical & Aerospace Engineering, George Washington University, 800 22nd St NW, Washington, DC 20052, USA

less thrust than their chemical counterparts and therefore orbital maneuvers have a much longer time of flight. In spite of this drawback, a wide variety of missions, such as communication and deep space probes, have utilized the unique benefits of low thrust electric propulsion to great effect [3].

Recent developments in miniature electric propulsion and small satellites now offer the potential for new research opportunities [6, 9]. The potential for more demanding missions places an even greater importance on the mission design to ensure that optimal trajectories satisfy mission requirements [6, 7, 14, 25]. There has been extensive research focused on the optimal control of spacecraft orbital transfers in the three-body problem [8, 14, 22, 25]. Within the three-body problem, a spacecrafts feasible region of motion is constrained by its energy, or Jacobi integral. The addition of low-thrust propulsion offers the potential of reduced transfer transit times and the ability to depart from the free motion trajectory to allow for increased transfer opportunities. Frequently, insight into the problem or intuition on the part of the designer is required to determine initial conditions that will converge to the desired solution due to the inherent nonlinear and chaotic behavior of the three-body system [28]. Conventional general-purpose Runge-Kutta integration techniques, such as those implemented in [8, 22], may fail to preserve geometric properties of the dynamic system numerically. Variational integrators can allow for reduced computational effort without any loss of numerical stability or energy drift which exist in conventional integration schemes.

Objective and Contribution

In this paper, we propose a systematic design method which enables low-thrust transfers in the planar circular restricted three-body problem. We utilize the concept of the reachability set to enable a simple methodology of selecting initial conditions to achieve general orbital transfers. The reachable set, defined as the set of all attainable states subject to the system constraints, allows for the extension of the previous control-free methods based on invariant manifolds. Defining the reachable set on a Poincaré section reduces the dimensionality of the system dynamics to the study of a related discrete update map. Through the use of low-thrust control input, the reachable set on the Poincaré section is enlarged and enables a larger space of potential transfers. By iteratively computing the reachable set, and minimizing the distance to the target on the Poincaré section, we generate general transfer trajectories. With this proposed method, the previous research on control-free trajectories will be generalized with the addition of low thrust propulsion systems.

In short, the authors present a systematic method of generating optimal transfer orbits in the three-body problem. This paper provides a discrete optimal control formulation to generate the reachability set on a Poincaré section.

In addition, the use of a geometric integrators ensures numerical stability for long-duration orbit transfers and maintains this behavior with the addition of small magnitude control inputs. Our computation of the reachable set allows for a simple metric of defining optimal trajectories. We avoid the issues inherent in selecting a valid initial condition for optimization. Rather, we choose a state on the reachability set which minimizes the distance toward the desired target. We demonstrate

these capabilities via two numerical examples simulating transfer trajectories in the Earth-Moon system.

Problem Formulation and Mathematical Background

We utilize the planar circular restricted three body problem (PCRTBP) as the basis of our system definition. It is a popular model in the preliminary analysis of multibody spacecraft trajectories. In the context of Earth based mission, the PCRTBP affords a relatively simple dynamic model while still capturing the major third body perturbation of the Moon. In addition, this model allows for a systematic process to define and exploit Poincaré sections. Furthermore, the 2D solutions afforded by the PCRTBP are frequently used to gain a qualitative understanding of the trade space of transfers in the Earth-Moon system. The PCRTBP approach offers insight into the fundamental dynamical structure while capturing the major dynamic properties of the planar motion. As a result, this approach is best suited for preliminary trajectories which do not require large plane changes.

The research in this work utilizes a variety of disparate concepts in dynamics, control theory, and astrodynamics. As a result, we briefly present some key concepts in the system model as well as established tools in the three body problem, such as invariant manifolds and Poincaré sections. In addition, we summarize the derivation of a variational integrator for the PCRTBP which is used in the subsequent geometric optimal control formulation.

Planar Circular Restricted Three Body Problem

The Earth is assumed to be the more massive primary, m_1, while the Moon is the second, smaller primary m_2. The equations of motion are developed in a rotating reference frame which allows for much greater insight into the structure of the dynamics. Following convention, the system is also non-dimensionalized by the characteristic units of length, mass, and time [14]. As a result, the system can be characterized by a single mass ratio parameter μ,

$$\mu = \frac{m_2}{m_1 + m_2}. \tag{1}$$

In the rotating reference frame the Lagrangian is given by

$$L = \frac{1}{2}\left((\dot{x} - y)^2 + (\dot{y} + x)^2\right) + \frac{1 - \mu}{r_1} + \frac{\mu}{r_2}, \tag{2}$$

where the distances $r_1, r_2 \in \mathbb{R}$ define the distance from the spacecraft to each primary and are defined as

$$r_1 = \sqrt{(x + \mu)^2 + y^2}, \tag{3}$$

$$r_2 = \sqrt{(x - 1 + \mu)^2 + y^2}. \tag{4}$$

Following a straightforward application of the Euler-Lagrange equations, a more detailed derivation is provided in [28], results in the following equations of motion defined in the rotating reference frame

$$\begin{bmatrix} \dot{r} \\ \dot{v} \end{bmatrix} = \begin{bmatrix} v \\ Av + \nabla U + u \end{bmatrix} = f\left(t, x, u\right) , \tag{5}$$

where the matrix A and pseudo gravitational potential gradient ∇U are

$$A = \begin{bmatrix} 0 & 2 & 0 \\ -2 & 0 & 0 \\ 0 & 0 & 0 \end{bmatrix}, \tag{6}$$

$$\nabla U = \begin{bmatrix} x - \frac{(1-\mu)(x+\mu)}{r_1^3} - \frac{\mu(x-1+\mu)}{r_2^3} \\ y - \frac{(1-\mu)y}{r_1^3} - \frac{\mu y}{r_2^3} \\ -\frac{(1-\mu)z}{r_1^3} - \frac{\mu z}{r_2^3} \end{bmatrix} = \begin{bmatrix} U_x \\ U_y \\ U_z \end{bmatrix}, \tag{7}$$

and the control input is defined as $u = \begin{bmatrix} u_x & u_y \end{bmatrix}^T \in \mathbb{R}^{2 \times 1}$ and assumed to be continuously variable but bounded in magnitude, i.e. $u^T u \leq u_{max}^2$. The state is defined as $x = \begin{bmatrix} r & v \end{bmatrix}^T$ with $r = \begin{bmatrix} x & y \end{bmatrix}^T \in \mathbb{R}^{2 \times 1}$ and $v = \begin{bmatrix} \dot{x} & \dot{y} \end{bmatrix}^T \in \mathbb{R}^{2 \times 1}$ representing the position and velocity with respect to the system barycenter, respectively.

Jacobi Integral

There exists a single integral, or constant of motion for the three-body problem [16, 28]. This energy constant is analogous to the total mechanical energy, however it is a non-physical quantity arising from the problem formulation [28]. Also known as the Jacobi constant, it is defined as a function of the position and velocity in the rotating frame and given by

$$E\left(r, v\right) = \frac{1}{2}\left(\dot{x}^2 + \dot{y}^2\right) - U\left(x, y\right) . \tag{8}$$

Equation 8 divides the phase space into distinct regions of allowable motion based on the energy level of the spacecraft. Fixing the Jacobi integral to a constant defines zero velocity curves, which are the locus of points where the kinetic energy, and hence velocity vanishes. As seen in Fig. 1, the phase space is divided into distinct realms based on the energy level. In the vicinity of m_1 or m_2 there exists a potential well. As the energy level increases there are five critical points of the effective potential where the slope is zero. Three collinear saddle points on the $\hat{e}_1$ axis and two equilateral points. These equilibrium, or Lagrange points, are labeled $L_i, i = 1, \ldots, 5$ and are shown in Fig. 1. The Jacobi integral is a valuable invariant property of the three-body system that allows for greater insight into the motion of the spacecraft.

Invariant Manifolds and Poincaré Map

Dynamics systems theory has been applied to the design of control-free maneuvers in the restricted three-body problem [14]. As previously introduced in Section
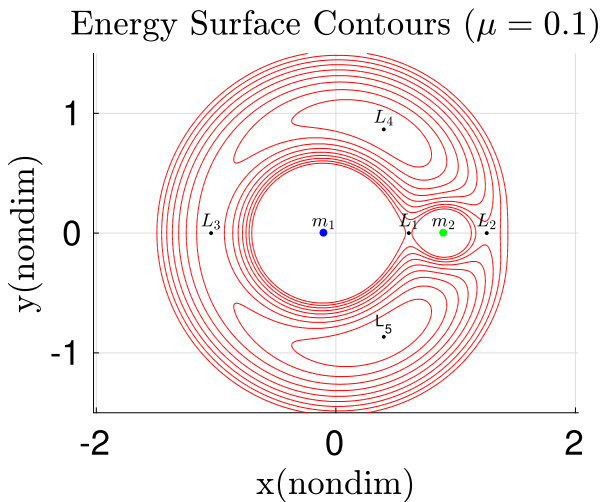
Fig. 1 Contour plot of Jacobi integral: Zero velocity curves of constant Jacobi integral. A particle with fixed energy level cannot cross the contour lines and is therefore limited to specific regions of the phase space

"Jacobi Integral", there exist five equilibrium points in the equations of motion for the three-body problem. It has been shown that the local orbit structure near the Lagrange points gives rise to families of periodic orbits as well as the stable and unstable manifolds of these periodic orbits. This rich structure is globally connected and gives rise to a dynamical chain which allows trajectories to pass through the phase space [4, 14]. The manifold structure associated with periodic orbits about the L_1 and L_2 Lagrange points are critical to the understanding of the motion of spacecraft as well as comets/asteroids. In addition, the stable and unstable manifolds serve as the boundaries of the phase space region that allow for the transport between realms in a single three-body system or between multiple three-body systems. These invariant manifolds only exist as a result of the dynamic formulation of the three-body problem in a rotating reference frame. Invariant manifolds serve as a higher dimensional generalization of the concept of seperatrices from linear systems as applied to the case of nonlinear systems.

Poincaré maps are a useful tool in the analysis of the flow near periodic orbits in the three-body problem. We let Σ define a hypersurface of section chosen such that all trajectories in the vicinity of a state $\boldsymbol{q} \in \Sigma$ cross Σ transversely and in the same direction. A Poincaré map, $P(\boldsymbol{q}) = \phi(T; \boldsymbol{q})$, maps the state of a trajectory from one intersection to the next. Choosing a section in this manner results in a Poincaré section as shown in Fig. 2. In Fig. 2 we show two examples of periodic trajectories intersecting the Poincaré section. Periodic solutions will appear as fixed points on the section, such as q_0, q_1 in Fig. 2, while stable or unstable trajectories become clearly visible by viewing successive intersections of the section. This allows for greater insight into the stability and dynamics of periodic solutions of a dynamic system as a fixed point on the Poincaré section corresponds to a periodic orbit while movement
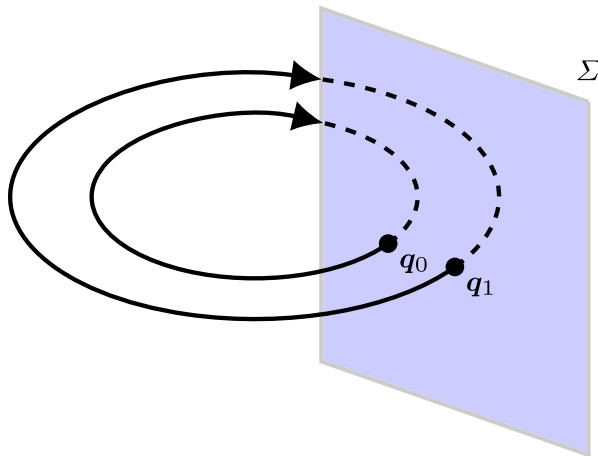
Fig. 2 Diagram of the Poincaré map: Periodic orbits will appear as fixed points on the Poincaré section Σ. Stability of periodic orbits is clearly visible on the section as successive intersections approach or depart a fixed point

on the section is associate with the stability of neighboring trajectories. For example, Poincaré maps have been used to prove the existence of homoclinic orbits, which are orbits both forward and backward asymptotic to a single unstable periodic orbit, and heteroclinic orbits, which join different periodic orbits [4, 13]. These dynamic features have been shown to play a vital role in the movement of natural bodies as well as critical for spacecraft missions [7, 18].

Combining invariant manifolds and an appropriate Poincaré section provides a conceptually simple manner to determine trajectories which connect wide regions of the phase space. However, the results previously developed are highly case specific and difficult to generalize to arbitrary transfers. Also, these results are based on control-free trajectories which rely on the underlying structure of the three-body system. In addition, transfer orbits along an invariant manifold require large time of flights which may be undesirable for time critical missions. The addition of low-thrust propulsion offers the potential of reduced transit times and the ability to depart from the free motion trajectory to allow for increased transfer opportunities. In this paper, we formulate an optimal control problem to generate the reachable set of the spacecraft. We compute the reachable set on an appropriate Poincaré section and use this to design a transfer trajectory.

Variational Integrator for PCRTBP

Geometric numerical integration deals with numerical integration methods which preserve the geometric properties of the flow of a differential equation, such as invariant properties and symplecticity. Variational integrators are constructed by discretizing Hamilton's principle rather than the continuous Euler-Lagrange equations. As a result, integrators developed in this manner have the desirable properties that they are symplectic and momentum preserving. In addition, they exhibit improved

energy behavior over long integration periods. A thorough discussion of variational integrators is provided in [21, 30]. We use this approach to construct a variational integrator for the PCRTBP with the inclusion of low-thrust propulsion.

Consider the autonomous mechanical system described by the Lagrangian, $L(q, \dot{q})$, for the generalized coordinates, q and velocities $\dot{q}$. The integration of the continuous Lagrangian along a path, $q(t)$, followed by the system must satisfy Hamilton's principle, which results in the well-known Euler-Lagrange equations [16]. In the discrete time scenario, the continuous path $q(t), \dot{q}(t)$, is replaced by a finite difference approximation over a fixed time step, e.g. q_0, $\frac{q_1 - q_0}{h}$, which converges to the true velocity as h tends towards zero. In this manner, we define a discrete Lagrangian, $L_d(q_0, q_1, h)$ which approximates the integral of the true Lagrangian over the time interval h between q_0 and q_1 [21].

The discrete equations of motion for the PCRTBP are derived by choosing an appropriate quadrature rule to discretize the continuous Lagrangian in Eq. 2 [21]. In this work, we apply the trapezoidal rule to approximate the action integral over a fixed time interval. The trapezoidal rule allows for a second order accurate approximation and alleviates the difficulties in applying implicit quadrature schemes. The discrete Lagrangian for the PCRTBP is given by

$$L_d = \frac{h}{2} \left(\frac{1}{2} \left[\left(\frac{x_{k+1} - x_k}{h} - y_k \right)^2 + \left(\frac{y_{k+1} - y_k}{h} + x_k \right)^2 \right] + \frac{1-\mu}{r_{1_k}} + \frac{\mu}{r_{2_k}} \right.$$
$$\left. + \frac{1}{2} \left[\left(\frac{x_{k+1} - x_k}{h} - y_{k+1} \right)^2 + \left(\frac{y_{k+1} - y_k}{h} + x_{k+1} \right)^2 \right] + \frac{1-\mu}{r_{1_{k+1}}} + \frac{\mu}{r_{2_{k+1}}} \right) . \text{(9)}$$

Applying a discrete version of the Lagrange-d'Alembert principle allows for inclusion of an external control force on the system [21]. Using Eq. 9 and some manipulation, gives the discrete equations of motion as

$$x_{k+1} = \frac{1}{1+h^2} \left[h\dot{x}_k + h^2 \dot{y}_k + x_k \left(1 + \frac{3h^2}{2} \right) + \frac{h^3}{2} y_k - \frac{h^3}{2} U_{y_k} - \frac{h^2}{2} U_{x_k} \right], \text{(10a)}$$

$$y_{k+1} = h\dot{y}_k + hx_k - hx_{k+1} + y_k + \frac{h^2 y_k}{2} - \frac{h^2}{2} U_{y_k}, \tag{10b}$$

$$\dot{x}_{k+1} = \dot{x}_k - 2y_k + 2y_{k+1} + \frac{h}{2}(x_{k+1} + x_k) - \frac{h}{2} U_{x_{k+1}} - \frac{h}{2} U_{x_k} + hu_x, \text{(10c)}$$

$$\dot{y}_{k+1} = \dot{y}_k + 2x_k - 2x_{k+1} + \frac{h}{2}(y_{k+1} + y_k) - \frac{h}{2} U_{y_{k+1}} - \frac{h}{2} U_{y_k} + hu_y. \text{(10d)}$$

The discrete equations of motion are given in the Lagrangian form after applying the discrete fiber derivative as $p_{x_k} = \dot{x}_k - y_k$ and $p_{y_k} = \dot{y}_k + x_k$. The state is defined as $\boldsymbol{x}_k = \begin{bmatrix} x_k & y_k & \dot{x}_k & \dot{y}_k \end{bmatrix}^T$ and the control input is $\boldsymbol{u} = \begin{bmatrix} u_x & u_y \end{bmatrix}^T$. This results in a discrete update map $f_k : \boldsymbol{x}_k \to \boldsymbol{x}_{k+1}$ which preserves the same properties

of the continuous-time dynamics in Eq. 5 such as invariants, symplecticity, and the configuration manifold. The discrete potential gradients are given by

$$U_{x_k} = \frac{(1-\mu)(x_k+\mu)}{r_{1_k}{}^3} + \frac{\mu(x_k-1+\mu)}{r_{2_k}{}^3}, \tag{11a}$$

$$U_{y_k} = \frac{(1-\mu)y_k}{r_{2_k}{}^3} + \frac{\mu y_k}{r_{2_k}{}^3}, \tag{11b}$$

$$U_{x_{k+1}} = \frac{(1-\mu)(x_{k+1}+\mu)}{r_{1_{k+1}}{}^3} + \frac{\mu(x_{k+1}-1+\mu)}{r_{2_{k+1}}{}^3}, \tag{11c}$$

$$U_{y_{k+1}} = \frac{(1-\mu)y_{k+1}}{r_{1_{k+1}}{}^3} + \frac{\mu y_{k+1}}{r_{2_{k+1}}{}^3}. \tag{11d}$$

The distances to each primary are defined as

$$r_{1_k} = \sqrt{(x_k+\mu)^2 + y_k{}^2}, \tag{12a}$$

$$r_{2_k} = \sqrt{(x_k-1+\mu)^2 + y_k{}^2}, \tag{12b}$$

$$r_{1_{k+1}} = \sqrt{(x_{k+1}+\mu)^2 + y_{k+1}{}^2}, \tag{12c}$$

$$r_{2_{k+1}} = \sqrt{(x_{k+1}-1+\mu)^2 + y_{k+1}{}^2}. \tag{12d}$$

Care must be taken during the implementation of Eq. 10a–d. As Eqs. 11a–d, and 12a–d are defined at both step k and $k+1$ they must be evaluated at both time instances. Equation 10a–d is implemented by first defining an initial state $\boldsymbol{x}_k$ and control $\boldsymbol{u}_k$. The distances and gravitational potential at step k are evaluated from Eqs. 11a, 11b, 12a and 12b. The discrete update steps in Eqs. 10a, and 10b are evaluated to generate x_{k+1} and y_{k+1}. Next, the distances and gravitational potential at step $k+1$ are evaluated from Eqs. 11c, 11d, 12c and 12d. Finally, the update steps in Eqs. 10c and 10d are evaluated. This results in the complete discrete update map $\boldsymbol{x}_k \to \boldsymbol{x}_{k+1}$ given $\boldsymbol{u}_k$.

Numerical Example

A simulation comparing the variational integrator to a conventional Runge-Kutta method is presented in this section. A particle is simulated from an initial condition of $\boldsymbol{x}_0 = \begin{bmatrix} 0.75 & 0 & 0.2 & 0 \end{bmatrix}^T$ for $t_f = 200 \approx 15$ years in the Earth-Moon system. The variational integrator uses a range of step sizes between 47.2–4720 s while the Runge-Kutta method uses a variable step size implemented via ODE45 in Matlab. The step size of the variational integrator is varied to approximately match the run time required by the conventional ODE45 integrator. Figure 3a shows the trajectory of the spacecraft in the rotating reference for this comparison. Both integration schemes result in trajectories that are initially nearly identical.

Figure 3b shows the mean Jacobi integral deviation over the entire simulation time as a function of computation time. For a given computational effort, in the form of simulation run time, the variational integrator will provide a smaller energy deviation as compared to the conventional integration scheme. Over long simulation horizons
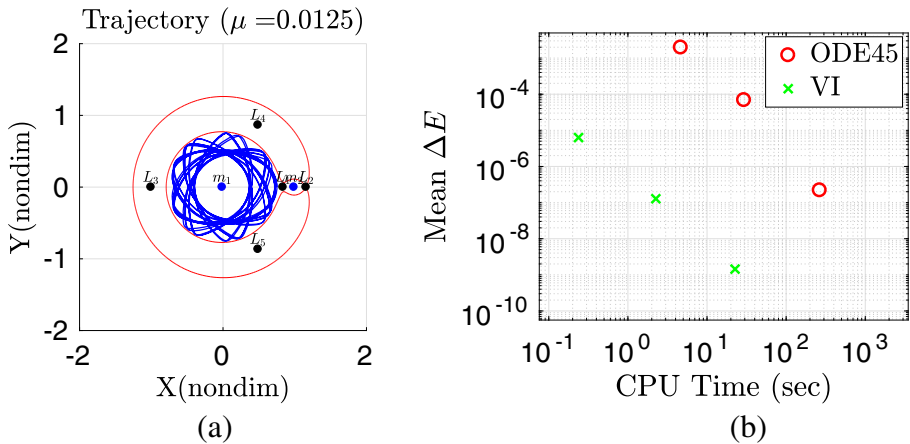
Fig. 3 **a** Earth-Moon three-body trajectory used for integrator comparison: A stable trajectory is used to test the variational and conventional integrators. The energy level is high enough to enter the vicinity of the Moon but not escape the three body system. **b** Mean Jacobi integral deviation between variational integrator and Matlab `ODE45`: A range of fixed step sizes are used for the variational integrator to approximately match the computational time of `ODE45`

or with the addition of small control inputs the inability of conventional integration schemes to accurately track the system energy limits the applicability of conventional techniques in which energy conservation is mandatory for characterizing the solution space. In spite of this improved energy behavior, the order and design of the variational integrator still play an important role in the accuracy of the state vector.

This work uses a second order integrator which has improved energy behavior in comparison to first order integration techniques without a significant increase in computational demand. The variational integrator is constructed according to a discrete version of Hamilton's principle, specifically for the given dynamic system, and it provides long-term structural stability in capturing the effects of low-thrust propulsion systems. General purpose numerical integrators, such as adaptive step-size Runge-Kutta methods may yield a more accurate state trajectory depending on the choice of integration parameters, but at the expense of additional computational demand and total energy deviations. However, for this preliminary analysis the variational integrator provides reduced computational demands, as compared with general-purpose numerical integrators with a similar level of numerical error, and is useful to characterize and explore the trade space in preliminary mission design scenarios. In addition, it has been shown that variable step integrators, such as `ODE45` in Matlab, tend to degrade first-order gradient based methods, such as those used in Section "Optimal Control Formulation" [24]. The presented results are based on the variational integrator with a fixed time step for numerical simulation and gradient computation. In summary, this paper utilizes the variational integrator to capture the long-term effects of low-thrust devices accurately and efficiently. The structural stability during numerical integration is critical for numerical optimization in the subsequent developments.

Optimal Control Formulation for Reachability Set

In this section, an optimal control formulation is presented to determine and design transfers within the three-body problem. The application of variational integrators to optimal control problems is referred to as computational geometric optimal control. Our formulation is based on the concept of the reachability set on a Poincaré section. This method allows one to easily determine potential transfer opportunities by finding set intersections on a lower dimensional space and greatly reduces the design process. The addition of continuous low thrust propulsion extends the control free design process developed previously and allows for a greater range of potential transfers with a reduced time of flight.

The numerical examples presented in this section are designed in the context of the PCRTBP. The dynamic environment has a four dimensional state space and offers a convenient integration constant in the form of the Jacobi integral. As a result, there are well defined methods to define and exploit Poincaré sections, which result in straightforward two-dimensional subspaces of the system. Our approach uses the Poincaré section to approximate the reachability set on this reduced subspace. As a result, this approach is more difficult to apply to three-dimensional transfers in the general three body problem. Poincaré sections in the case of the general six dimensional state space are significantly more challenging and typically require more complicated visualization techniques. However, this is an area of active research and some of the authors future research is aimed at implementing this approach for non-planar transfer trajectories [15].

Reachability Set

Reachability theory provides a framework to evaluate control capability and safety. The reachable set contains all possible trajectories that are achievable over a fixed time horizon from a defined initial condition, subject to the operational constraints of the system. Reachability theory has been applied to aerospace systems such as collision avoidance, safety planning, and performance characterization. The theory formally supporting reachability has been extensively developed and is directly derivable from optimal control theory [19, 20, 29]. More recently, reachability theory has recently been applied to space systems [5, 10, 12]. Computation of the reachable set for a system involves solving the Hamilton-Jacobi partial differential equation or satisfying a dynamic programming principle. Analytical computation of reachable sets is an ongoing problem and is only possible for certain classes of systems. Typically, numerical methods are used to generate approximations of the reachability set, but are generally limited by the dimensionality of the problem.

Computation of reachable sets is critical to space situational awareness, rendezvous and proximity operations, and orbit determination operations. Specifically, maintaining accurate estimates of a spacecraft state over extended periods is not trivial. The challenge is increased for multiple spacecraft operating in close proximity or when there are long periods of time between measurements. Coupling the ability for continuous low-thrust propulsion between measurements increases the

measurement association complexity. Computing the reachability set given estimated states and control authorities allows one to better correlate subsequent measurements or determine sensor pointing regions in the event of a lost spacecraft.

Optimal Control Formulation

In this paper, we seek to approximate the reachability set on a Poincaré section by solving a related optimal control problem. We choose our Poincaré section in a similar manner to those used previously for the design of transfers via invariant manifolds. The Poincaré section is chosen to intersect transversally with trajectories emanating from the initial orbit. In the case of a periodic orbit the trajectories will cross the Poincaré section at two distinct fixed points every half period. The main idea is that the addition of low thrust propulsion allows us to enlarge the set of trajectories achievable in the Poincaré section. Figure 4 illustrates how, without any control input, trajectories will intersect with the Poincaré section at x_n. However, the addition of low thrust propulsion allows the spacecraft to depart from the natural dynamics and intersect the Poincaré section at a different location. We use a cost function to define a distance metric on the Poincaré section from the control-free intersection to an intersection under the influence of the control input. Maximization of this distance along varying directions enables us to generate the largest reachability set under the bounded control input. In Fig. 4 the reachable set is shown as a circular region on the Poincaré section. In practice, the reachable set will be of a general shape and also higher dimensional in the nonplanar case.
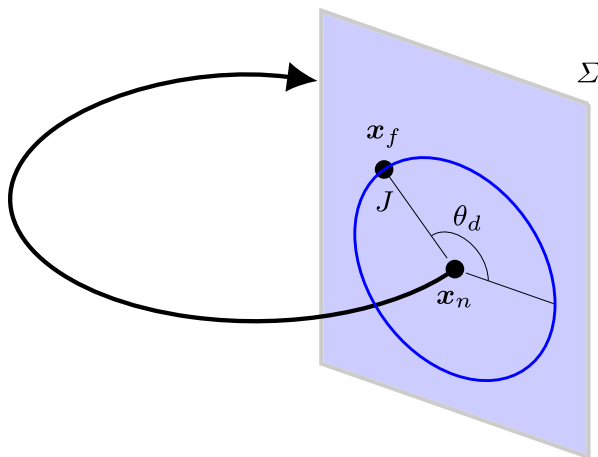

Fig. 4 Reachability set on a Poincaré section: Pictorial representation of the reachability set (blue circle) on the Poincaré section, Σ. The terminal state, x_n, is the intersection without any control input. Adding a control input allows for the terminal state, x_f, to be displaced by some distance/cost J as measured on the section. We parameterize a specific direction on the section with the angles θ_d and seek to maximize the distance between x_f and x_n. Computation of the maximum distance, or reachability, for a variety angles gives a discrete approximation of the reachability set. In general, the reachable set can be an arbitrary shape on the section rather than the circular set depicted

We define the Poincaré section along the horizontal axis, which is equivalent to the surface $y = 0$, and given by

$$\Sigma = \{(x, \dot{x}) \mid y = 0\}. \tag{13}$$

This is similar to the previous work in determining homoclinic orbits in the three-body problem [14, 17]. Previous analytical results have shown that homoclinic orbits intersect transversally in the $(x, \dot{x})$ space on the plane $y = 0$. We seek to compliment these results with the addition of low thrust propulsion to maximize the reachable set on the Poincaré section. Placing our section at $y = 0$ ensures that all trajectories will intersect our section. An optimal control problem is defined by a cost function

$$J = -\frac{1}{2} (\boldsymbol{x}(N) - \boldsymbol{x}_n(N))^T \begin{bmatrix} 1 & 0 & 0 & 0 \\ 0 & 0 & 0 & 0 \\ 0 & 0 & 1 & 0 \\ 0 & 0 & 0 & 0 \end{bmatrix} (\boldsymbol{x}(N) - \boldsymbol{x}_n(N)) = \phi(\boldsymbol{x}(N), \boldsymbol{x}_n(N)). \tag{14}$$

The term $\boldsymbol{x}_n(N)$ is the final state of a control-free trajectory while the term $\boldsymbol{x}(N)$ is the final state under the influence of the control input. Maximization of the distance between $\boldsymbol{x}_n$ and $\boldsymbol{x}$, on the Poincaré section defined in Eq. 13 at the terminal time $t_f = N$, is equivalent to the minimization of J defined in Eq. 14. The Poincaré section is defined through the use of appropriate terminal constraints given by

$$v_1(\boldsymbol{x}(N)) = y(N) = 0, \tag{15a}$$

$$v_2(\boldsymbol{x}(N)) = \frac{\dot{x}(N) - \dot{x}_n(N)}{x(N) - x_n(N)} - \tan \theta_d = 0, \tag{15b}$$

$$0 \geq \boldsymbol{u}^T \boldsymbol{u} - u_{max}^2, \tag{15c}$$

where the angle θ_d defines a direction in which we wish to maximize the reachability set on the Poincaré section. The maximum control thrust magnitude is defined by u_{max} and is non-dimensionalized by the characteristic units of length, mass, and time. The goal is to determine the control input $\boldsymbol{u}_k$ such that the cost function (14) is minimized subject to the state equations of motion (10a–d) and constraints (15a–c).

Application of the Euler-Lagrange equations allows us to derive the necessary conditions for optimality [1]. The discrete variational integrator in Eq. 10a–d is used rather than the continuous time counterpart. This results in a discrete optimal control problem and the discrete necessary conditions are given as

$$\boldsymbol{\lambda}_{k+1}^T = \boldsymbol{\lambda}_k^T \left(\frac{\partial \boldsymbol{f}_k}{\partial \boldsymbol{x}_k} \right)^{-1}, \tag{16a}$$

$$0 = \frac{\partial H_k}{\partial \boldsymbol{u}_k}, \tag{16b}$$

$$0 = \frac{\partial \phi}{\partial \boldsymbol{x}_k}^T + \frac{\partial \boldsymbol{v}}{\partial \boldsymbol{x}_k}^T \boldsymbol{\beta} - \boldsymbol{\lambda}^T(N), \tag{16c}$$

where the Hamiltonian H is defined as

$$H_k = \boldsymbol{\lambda}_k^T \boldsymbol{f}(\boldsymbol{x}_k, \boldsymbol{u}_k), \tag{17}$$

and $\boldsymbol{\lambda} \in \mathbb{R}^{4 \times 1}$ is the costate and $\boldsymbol{\beta} \in \mathbb{R}^{2 \times 1}$ are the additional Lagrange multipliers associated with the terminal constraints in Eq. 15a–c. The state dynamics are represented by $\boldsymbol{f}(\boldsymbol{x}_k, \boldsymbol{\lambda}_k)$ after substituting (16b) into Eq. 10a–d. This indirect optimal control formulation leads to a two point boundary value problem with split boundary conditions. By sweeping the angle θ_d one can approximate the reachable set on the Poincaré section subject to the bounded control input.

The costate equation of motion requires the Jacobian of Eq. 10a–d and is given by

$$\boldsymbol{\lambda}_{k+1}^T = \boldsymbol{\lambda}_k^T \begin{bmatrix} f_{1_x} & f_{1_y} & f_{1_{\dot{x}}} & f_{1_{\dot{y}}} \\ f_{2_x} & f_{2_y} & f_{2_{\dot{x}}} & f_{2_{\dot{y}}} \\ f_{3_x} & f_{3_y} & f_{3_{\dot{x}}} & f_{3_{\dot{y}}} \\ f_{4_x} & f_{4_y} & f_{4_{\dot{x}}} & f_{4_{\dot{y}}} \end{bmatrix}^{-1} . \tag{18}$$

The derivation of Eq. 18 is given in Appendix. In addition, the computation of Eq. 18 requires inversion of the Jacobian matrix. This is a computationally expensive operation that is prone to numerical error and instability. We use Gauss-Jordan elimination to avoid this inversion in Eq. 18 and determine an explicit update map $\boldsymbol{\lambda}_k \rightarrow \boldsymbol{\lambda}_{k+1}$.

The optimal control formulation presented in this section results in a two point boundary value problem (TPBVP). There exist many methods to solve TPBVPs such as gradient, quasilinearization, and shooting methods [1, 11]. Shooting methods are common in astrodynamic trajectory design problems and relatively simple to implement. In the shooting method, initial conditions are varied such that a terminal constraint is satisfied, similar to the way an archer modifies the bow in order to more accurately strike a target. Consider the vector of initial conditions, $\boldsymbol{\chi} = \{\boldsymbol{x}_0, \boldsymbol{\lambda}_0\}$, which is varied to satisfy some terminal constraints of the form $\boldsymbol{G}(\boldsymbol{\chi}) = \{\boldsymbol{x}_t - \boldsymbol{x}_n\} = 0$. The free variables at the terminal time are computed by propagation of $\boldsymbol{\chi}$ over the selected time horizon. At the terminal time, the constraint vector is calculated and if not satisfied $\boldsymbol{\chi}$ is varied. Rather than numerical integration over the entire time interval, multiple shooting segments the interval into several smaller sub-arcs [27]. This multiple shooting approach incorporates additional interior constraints but reduces the sensitivity of the costates along each sub-arc. The use of the multiple shooting method reduces the sensitivity of changes in the initial costate at the expense of
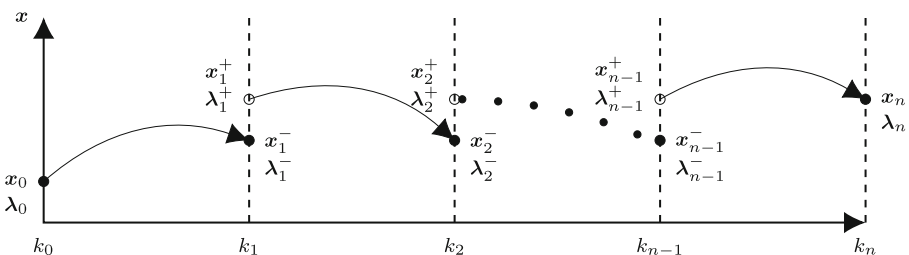

Fig. 5 Schematic diagram of the multiple shooting method: The complete trajectory is split into a number of sub-segments, and additional interior constraints are included to ensure state and costate continuity. Splitting the optimal trajectory into short segments reduces the sensitivity of terminal states to variations of the initial states

additional design variables, but has been shown to provide more stable and robust solutions [23].

In Fig. 5, we show a schematic representation of the multiple shooting procedure. We split the optimal control horizon into equal length subsegments such that the length of each segment is $\frac{k}{n}$, where k, n are the total number of steps and number of stages, respectively. Similarly, we divide the state and costate trajectories into n equal segments. To ensure continuity, additional interior constraints are incorporated as

$$\boldsymbol{x}_1^- - \boldsymbol{x}_1^+ = 0, \tag{19a}$$

$$\boldsymbol{\lambda}_1^- - \boldsymbol{\lambda}_1^+ = 0, \tag{19b}$$

$$\boldsymbol{x}_2^- - \boldsymbol{x}_2^+ = 0, \tag{19c}$$

$$\boldsymbol{\lambda}_2^- - \boldsymbol{\lambda}_2^+ = 0, \tag{19d}$$

$$\vdots$$

$$\boldsymbol{x}_{n-1}^- - \boldsymbol{x}_{n-1}^+ = 0, \tag{19e}$$

$$\boldsymbol{\lambda}_{n-1}^- - \boldsymbol{\lambda}_{n-1}^+ = 0. \tag{19f}$$

Using the multiple shooting method reduces the sensitivity of the terminal states, $\boldsymbol{x}_i^+, \boldsymbol{\lambda}_i^+$, to variations of the initial states, $\boldsymbol{x}_{i-1}^-, \boldsymbol{\lambda}_{i-1}^-$. As a result, the design vector $\boldsymbol{\chi}$ is augmented with the additional interior initial conditions, $\boldsymbol{x}_i^-, \boldsymbol{\lambda}^-$. Similarly, the constraint vector is augmented with the additional interior constraints defined in Eq. 19a. Based on experimentation, we use four stages in our multiple shooting method. This provided the best performance and convergence stability while minimizing the difficulties in additional interior constraints. The multiple shooting algorithm now varies the design vector $\boldsymbol{\chi}$ to ensure that the constraints in $\boldsymbol{G}(\boldsymbol{\chi})$ are satisfied. In this work, we use the Matlab nonlinear solver `fsolve` to solve the system of nonlinear equations defined by the multiple shooting algorithm with a convergence tolerance of 1×10^{-5}. Within `fsolve`, we use the trust-region dogleg solver which makes use of the Powell dogleg procedure for computing a step direction and magnitude to minimize successive iterations of the solver. All numerical integration is performed using the discrete variational integrator described in Section "Variational Integrator for PCRTBP". The numerical results are specific to the choice of nonlinear solver, and different tolerances or software tools may result in slight changes.

Numerical Example

We present two numerical simulations in the Earth-Moon system to demonstrate the transfer procedure. These simulations enable the spacecraft to depart from the natural dynamics through the use of low-thrust propulsion. The reachability set on the Poincaré section allows for a straightforward method of determining transfer opportunities. The first example is a transfer from a periodic orbit of the L_1 Lagrange point to a fixed orbit of the moon. This example uses a single iteration of the reachable set

computation in the design of the transfer. The second example is a transfer from geostationary orbit of the Earth to a period orbit of L_1. This examples demonstrates the ability to extend the reachability process to multiple iterations, to allow for a much larger and more general transfer. With both examples it is possible to depart from the vicinity of the Earth to a Moon orbit via a series of reachable sets defined on Poincaré sections. The numerical examples presented in this section satisfy the necessary conditions for local optimality and obtaining a globally optimal solution is considered beyond the scope of this paper.

Periodic Orbit transfer

The first objective is to design a transfer trajectory from a planar periodic orbit about the L_1 Lagrange point to a bounded orbit in the vicinity of the Moon. The target region is created by choosing an initial condition of $x_0 = \begin{bmatrix} 1.05 & 0 & 0 & 0.35 \end{bmatrix}^T$ with $\mu = 0.0125$. The target set is propagated over a period of $t = 20$ in non-dimensional units which corresponds to approximately 1.5 years. Figure 6 shows that the target set remains in the vicinity of the Moon, or m_2, in the rotating reference frame. This type of orbit would be useful for a variety of mission scenarios. For example, a series of communication satellites could be placed in this type of orbit. The bounded trajectories of the vehicles and constant line of sight to both the Moon and the Earth would allow for constant communication for future manned missions and potential habitats. The initial set is a planar periodic orbit about L_1, which is generated using the process of differential correction of a linear approximation [14].

As a source for comparison, the method of using invariant manifolds, introduced in [14], is implemented. As described in Section "Invariant Manifolds and Poincaré Map",
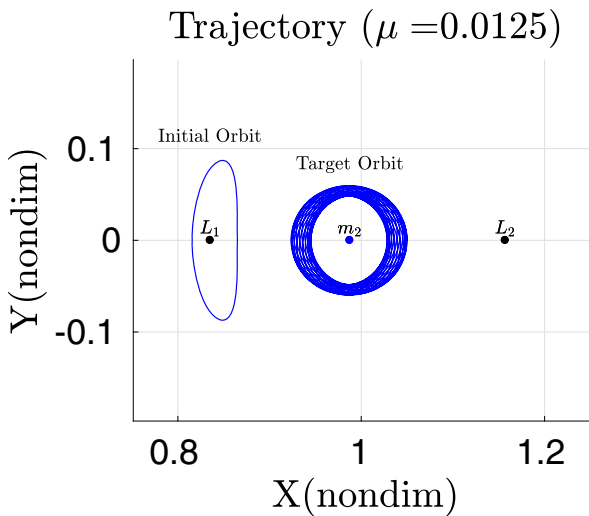

Fig. 6 L_1 periodic orbit transfer to orbit of the Moon: Example scenario demonstrating the initial and target orbit. Without the low-thrust propulsion, the spacecraft is constrained to the initial periodic orbit. We determine the reachability set to find a transfer trajectory to the target orbit about the moon

these invariant manifolds are the set of trajectories that either asymptotically arrive or depart the periodic orbit. We generate the unstable manifold associated with the initial planar periodic orbit. We numerically propagate the unstable manifold forward in time until the trajectories intersect the Poincaré section $y = 0$. Figure 7a shows the unstable invariant manifold generated from the initial L_1 periodic orbit. The blue points in Fig. 7b are the intersections of the target Moon orbit and the Poincaré section. The two circular regions are the ascending (right) and descending (left) intersections of the target orbit and Poincaré section. The green points in Fig. 7b are intersections of the unstable manifold from Fig. 7a with the Poincaré section $y = 0$. Only a single branch of the invariant manifold intersects with the ascending region of the target orbit. There are no intersections of the invariant manifold with the descending region of the target orbit. The numerical values associated with the green points denote the required time of flight along the invariant manifold in non-dimensional units. The required travel time for a transfer using the unstable invariant manifold is approximately $t_f \approx 3.1$ non-dimensional time units.

Next, we determine the reachability set with addition of a low-thrust control input over a fixed time horizon. In Section "Reachability Set on the Poincaré Section", we demonstrate the effect of variations in the choice of maximum control bound and terminal time. While Section "Transfer to Periodic Orbit" show a specific example of a transfer design process using the intersection of the reachability set on the Poincaré section. The analysis presented in the following sections define a maximum magnitude of the thrust as u_m and assume that the trust can be directed arbitrarily within the plane. This model is representative of many spacecraft which have a body fixed thruster and attitude control system. Assuming a fully actuated spacecraft model allows us to decouple the translation and rotational dynamics of the spacecraft.

(a) Position space view of invariant manifold

(b) Poincaré intersection of invariant manifold (green), target orbit (blue) and the initial orbit (black)
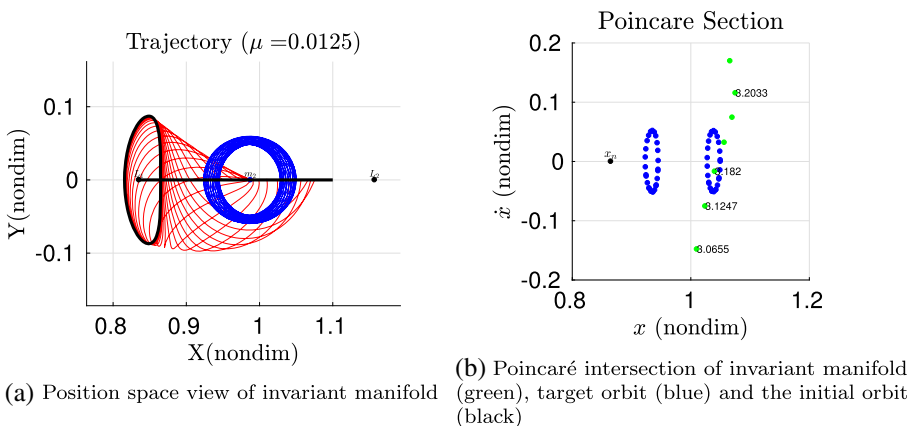
Fig. 7 Invariant manifold transfer: An example transfer using the invariant manifolds is shown in both the position and Poincaré spaces. The control free transfer from the initial periodic orbit to the target orbit result in a long time of flight. In addition, the manifold only intersects the target orbit on the ascending or far side of the moon

Table 1 Combinations for t_f and u_m used to generate the reachability sets in Fig. 8

| t_f	u_m
1.24	0.05
1.30	0.25
1.37	0.5
1.44	

Reachability Set on the Poincaré Section

From the initial state on the periodic orbit, a series of optimal trajectories are generated to determine the reachable set. The multiple shooting approach is implemented to solve the optimal control problem. We divide the time horizon into two equal length segments. The state trajectory is initialized using the free trajectory of the periodic orbit. Similarly, the costate trajectory is initialized from an initial guess of $\boldsymbol{\lambda}_0 = \begin{bmatrix} -1 & -1 & -1 & -1 \end{bmatrix}^T$ and propagated using the discrete equations of motion in Eq. 18. This results in the initial guess of the design vector $\boldsymbol{\chi} = \begin{bmatrix} \boldsymbol{\lambda}_0 & \boldsymbol{x}_1^- & \boldsymbol{\lambda}_1^- & \boldsymbol{\beta} \end{bmatrix}^T$. This design vector is then varied to ensure that the necessary conditions of optimality and the interior point constraints are satisfied. Table 1 shows the range of terminal times, t_f, and maximum control bound, u_m, which are used to investigate their effect on the subsequent reachable set on the Poincaré section.

The angle θ_d in Eq. 15a–c is varied to select a different direction along the Poincaré section to maximize. We discretely vary the angle over the range $0° \leq \theta_d < 360°$ to approximate the reachability set of the spacecraft. Choosing a new angle θ_d corresponds to a different direction as well as a new optimal control problem which is again solved using the multiple shooting approach laid out previously. Each optimal control solution, corresponding to a discrete value of θ_d, is solved using `fsolve` as described earlier. Each solution on the reachability set is computed in approximately 2 min on a desktop computer using an 3.4 GHz Intel i7-3700. The intersection of the optimal trajectories as well as those of the target Moon orbit with the Poincaré section are shown in Fig. 8.

Figure 8 shows the reachabilty set for twelve combinations of t_f and u_m listed in Table 1. With a small maximum control bound, $u_m = 0.05$ shown using square markers, the reachable set is not dramatically changed from that of the no control solution. The reachable set is denoted using square markers on the left most portion of Fig. 8b. Variations of t_f are indicated using different colors and also demonstrate that this parameters has a smaller impact than changes in u_m. Increasing the control bound to $u_m = 0.25$ and $u_m = 0.5$ shows that the reachable set progressively approaches the target set.

The reachable sets presented in Fig. 8 are highly dependent on the initial condition, terminal time, and maximum control bound. This example demonstrates that increasing the u_m results in a larger displacement between the controlled and uncontrolled trajectories. The reachable set is enlarged from a single point, as shown in Fig. 7b by the black point, to a larger region as shown in Fig. 8b. The choice of u_m, t_f and initial condition all combine to change the resulting reachability set.
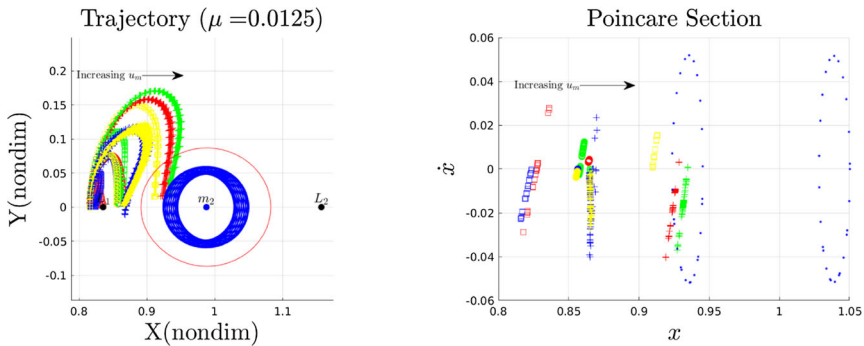
(a) Position space view of reachability sets   (b) Poincaré section view of reachability sets

Fig. 8 Variation of t_f and u_m on the reachability set. Colors, {red}, blue, green, yellow}, are used note increasing t_f while markers, {circle, square, cross}, are used to denote increasing u_m. Increasing the maximum control bound has a large effect and enables the reachability set to intersect the target manifold. Increases in t_f are less critical and have minimal impact on the distribution of the reachability set on the Poincaré section

Transfer to Periodic Orbit

Here we use the results of the preceding section to demonstrate one specific example of a transfer designed using the reachability set. The acceleration limit is chosen as $u_{max} = 0.75 \approx 2\,\text{mm s}^{-2}$ in the Earth-Moon system. Assuming a fixed spacecraft mass of 500 kg, this model defines a maximum thrust of approximately 1 N. Currently, the NASA NEXT xenon thruster is able to provide approximately 0.25 N of thrust, and a cluster of such engines could be used to provide the desired thrust used in this work [26]. The trajectories are generated from a fixed initial state of $\boldsymbol{x}_0 = \begin{bmatrix} 0.8156 & 0 & 0 & 0.1922 \end{bmatrix}^T$ over a fixed time span of $t_f = 1.4$. This initial state lies on the initial periodic orbit and the time of flight is equivalent to one half period of the initial periodic orbit.

The optimal trajectories, under the influence of the control input $\boldsymbol{u}$, are plotted in red in Fig. 9a. Initially, the spacecraft is assumed to lie on the periodic orbit. As a result, the intersection of this periodic orbit with the Poincaré section are two points corresponding to the two crossing of the orbit. We show the control-free intersection, $\boldsymbol{x}_n$, of the periodic orbit on the Poincaré section in Figs. 7b and 9b The use of the continuous low thrust propulsion expands the reachable set to region bounded by the red markers in Fig. 9b. The reachable set is an ellipsoidal region with a major axis aligned along $\theta \approx 70°$ as compared to a fixed point without any control input.

Figure 9b shows that the reachable set and those of the descending target region intersect. As both regions are discretely approximated a linear interpolation is used to determine the exact intersection state on the Poincaré section. This intersection generates a partial target state of $x_t, \dot{x}_t$ and $y = 0$ from the Poincaré section. Using the energy level of the target region, defined by Eq. 8, and the intersection state we can calculate the final component $\dot{y}$. This results in a complete target state $\boldsymbol{x}_t$ which

(a) Position space view of reachability set

(b) Poincaré section view of reachability set

(c) Transfer trajectory selected from reachability set viewed in the position space

(d) Control input for the selected transfer trajectory
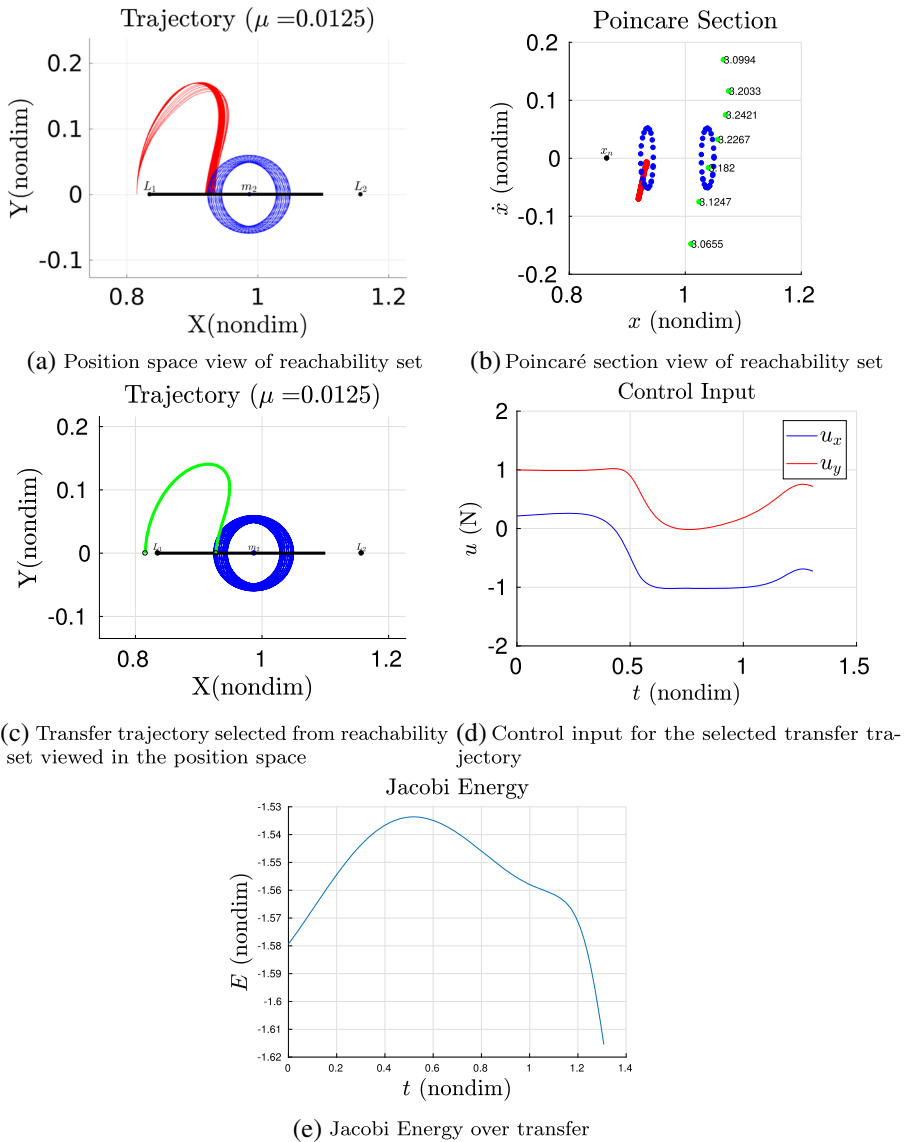

(e) Jacobi Energy over transfer

Fig. 9 L_1 Reachability set transfer: The low thrust propulsion is used to approximate the reachability set starting from the initial periodic orbit over a fixed time horizon. The reachability set is shown in Fig. 9a and b in both the position and Poincaré space respectively. From this reachability set we chose a trajectory which intersects the target orbit and it is shown in Fig. 9c. The optimal control to achieve this transfer is shown in Fig. 9d

lies on the reachable set and on the target orbit. Due to the use of low-thrust propulsion, there is a change in Jacobi energy during the transfer as the vehicle transitions between the initial and final periodic orbits. This behavior is demonstrated in Fig. 9e as the vehicles experiences an increase in energy transitioning towards the target followed by a decrease to arrive at the target.

A final optimal trajectory is generated such that the $x(N) = x_t$. This transfer serves to satisfy a required boundary condition to ensure a continous trajectory to the target. The reachability set, and the intersection on the Poincaré section, are used to generate a partial target state for the transfer. Due to the difference in Jacobi energy, a final optimal transfer is computed to satisfy the desired target state. This transfer trajectory is denoted by the green path in Fig. 9c. The optimal control input is shown in Fig. 9d. The spacecraft achieves the desired target while satisfying the bounded control input. The Jacobi energy integral, computed using Eq. 8, is shown in Fig. 9e. Figure 9e shows that the vehicle begins with an energy level equal to the periodic orbit and arrives at the target orbit with the appropriate energy. The first half of the transfer is associated with and increase in energy as the control is used to transition towards the target orbit which is followed by a energy decrease to the target orbit. This roughly corresponds with the expected optimal solution of a bang-coast-bang type orbital transfer [11]. Convergence statistics associated for this transfer are shown in Table 2.

A transfer along the invariant manifold requires on average $t_f \approx 3.1$ as compared to $t_f \approx 1.4$ for a transfer using low thrust propulsion and the reachable set. This long time of flight is typical of transfers using invariant manifolds. The unstable invariant manifold traverses a large region of the phase space and is dependent on the system dynamics. In addition, the invariant manifolds asymptotically arrive and depart from the periodic orbit. As a result, it may take an arbitrarily long period of time to depart from the vicinity of the periodic orbit. In addition, only a small portion of the invariant manifold intersects with the target Moon orbit. In contrast, the low thrust control input we are able to enlarge the reachability set from a single point, x_n associated with the periodic orbit, to a larger ellipsoidal region shown in red in Fig. 9b. This achieves an intersection with the target orbit with a much lower time of flight as compared to the invariant manifold method. In addition, by generating the reachability set we are able to compute the required control input to exactly intersect the target orbit. This avoids having to compute and accomplish a secondary impulsive maneuver to transition from the invariant manifold to the target orbit.

Geostationary Transfer

There are many situations where a more complicated and extensive orbital transfer is desired. In this section, we present a simulation of transferring from a geostationary

Table 2 Convergence statistics for the periodic orbit transfer

Metric	Value
`fsolve` objective	6.03×10^{-15}
`fsolve` major iterations	9
`fsolve` first order optimality	1.88×10^{-13}
Optimal cost	2.09×10^{-31}
Execution time	1.49 s

orbit to a periodic orbit about the L_1 Lagrange point. From this location, it is possible to transition to the Moon, as shown in Section "Periodic Orbit transfer", or beyond the Earth-Moon system through the use of invariant manifolds [14]. This type of low energy transfer would be most suitable for unmanned spacecraft transitioning from the Earth to the Moon. The long time of flight would make such a transfer unsuitable for manned missions due to life support constraints. Future proposals for permanent lunar spacecraft and bases will require frequent supply missions to remain viable. Transfers from the Earth to the Lagrange points, through the use of low-thrust electric propulsion, offer an additional and potentially shorter time of flight in comparison to the low-energy transfers which utilize solar perturbations.

Section "Periodic Orbit transfer" demonstrated the capability of determining an orbital transfer after locating the intersection of the reachability set and a target orbit. However, it may not be possible to achieve an intersection on the Poincaré section after a single iteration. Since the spacecraft has an upper bounded control input and time of flight the reachability set is finite in size. As a result, we present a method of performing several iterations of the reachability set computation. A straightforward method is presented which allows for a series of reachability sets to be computed which progressively move the trajectory towards the target. In this manner, it is possible to determine more complicated transfers by a simple selection of states from the reachability set. This affords a systematic method of determining general transfer trajectories in the three body problem.

It is possible to design arbitrary transfers using either a direct optimization or invariant manifold based approach. The direct optimization method transforms the optimal control problem into a nonlinear programming problem. Instead of solving the Euler-Lagrange equations the state and control histories are parameterized and solved through any number of mathematical programming methods. However, due to this parameterization only an approximate solution, which approximates the true optimal solution in the limit, is feasible. On the other hand, our method applies an indirect optimization method. The necessary conditions for optimality are computed and directly solved in generating the reachability set. The use of the reachability set also avoids the issues of selecting a valid initial condition. We select a state on the maximum reachability set which minimizes the distance toward the target. This straightforward approach achieves an optimal trajectory and is used to generate general transfers.

The invariant manifold method is difficult to apply to general orbital transfers. The manifolds are associated with periodic orbits in the three-body system. In this case, an appropriate periodic orbit must first be determined prior to generating the invariant manifold. Furthermore, there is no guarantee that the invariant manifold will pass through a desired region of space. For example, in the Earth-Moon system the unstable manifolds of periodic orbits about L_1 do not pass close to the Earth, but rather are beyond the geostationary orbit altitude. In addition, determining the intersections between various invariant manifolds is not trivial. It requires an appropriate Poincaré section and the generation of several invariant manifolds. There is no clear method of selecting the periodic orbits required based on the type of transfer desired. Determining an intersection between these invariant manifolds generally requires extended flight times, involving several orbits of the primaries, before an appropriate

intersection is found. As a result, it is difficult to generalize this method to arbitrary transfers in the three-body problem.

This numerical simulation demonstrates the ability of the our approach to determine more general transfer trajectories in the PCRTBP. We use multiple iterations of the reachability set to achieve a more complicated transfer. In this manner, it is possible to design arbitrary transfers which are not possible using a single reachability computation. Initially, it is assumed that the spacecraft lies on a circular geostationary orbit in the non-dimensional Earth-Moon three-body system. While the geostationary orbit is not a typical "parking orbit" for most spacecraft missions it serves as a convenient altitude to demonstrate our approach. The geostationary orbit about the Earth is transformed into the rotating reference frame of the Earth-Moon three body problem. In addition, we non-dimensionalize the initial state to find $x_0 = \begin{bmatrix} 0.0972 & 0 & 0 & 3.0010 \end{bmatrix}^T$ as the initial condition of the spacecraft on the geostationary orbit. It is desired to transfer to a periodic orbit about the L_1 Lagrange point. The periodic orbit is defined by the initial condition $\begin{bmatrix} 0.8057 & 0 & 0 & 0.2982 \end{bmatrix}^T$. The initial and target orbits are illustrated in Fig. 10. In Fig. 10, the initial orbit is located in the center of the figure and centered about m_1 while the target periodic orbit is determined about the L_1 Lagrange point. Instead of determining a transfer directly between the geostationary orbit and the periodic orbit, we seek to instead transfer to the stable manifold of the periodic orbit. This stable manifold will then asymptotically approach the target orbit without any further control input. Once on the manifold, the spacecraft will coast in an uncontrolled fashion and asymptotically arrive at the desired periodic orbit.

We first generate the stable invariant manifold associated with the periodic orbit in order to determine our target set. The stable manifold is propagated to the Poincaré
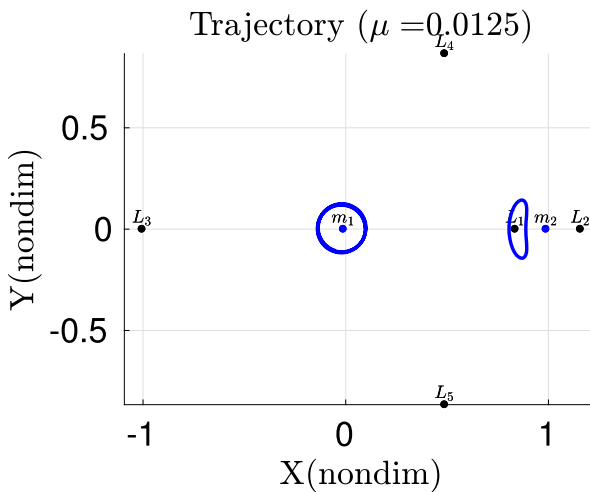

Fig. 10 Geostationary to L_1 transfer: Representation of the initial and target orbits for the reachability transfer. Vehicle is assumed to begin on the geostationary orbit about m_1 and will transfer to the periodic orbit about L_1

section at $y = 0$, which is denoted by the horizontal black line in the position space visualizations given in Figs. 11, 12 and 13a. The stable manifold is denoted by the green trajectories which span the majority of the phase space. In addition, we plot the intersection of the stable manifold with the Poincaré section with green markers. The initial orbit and the stable invariant manifold do not intersect and the transfer objective is to enlarge the reachability set to include the stable manifold.

Next, we compute the reachable sets originating on the geo-stationary orbit and subject to the maximum control constraint. The multiple shooting approach is used to solve the optimal control problem with two segments. For the first reachability set computation, the initial geostationary orbit is used to initialize the multiple shooting algorithm. We use the same initial guess of $\boldsymbol{\lambda}_0$ as in Section "Periodic Orbit transfer" and propagate over the fixed time horizon of the period of the geostationary orbit to initialize $\boldsymbol{\lambda}_i^-$.

The first reachable set is computed beginning on the geostationary orbit at it's intersection with the Poincaré section and we again assume a upper bound on the thrust magnitude of $u_{max} = 0.75$. The reachable set is generated by varying the angle $0° \leq \theta < 360°$ in Eq. 15a–c defined on the Poincaré section. This allows us to approximate the set of states that are achievable in the $(x, \dot{x})$ space. The intersection of the first reachable set with the Poincaré section is shown in Fig. 11b in red. While the reachable set does not intersect the stable manifold, it does reduce some of the distance in the $\dot{x}$ dimension. From this reachable set, we chose a trajectory which minimizes the distance towards the stable manifold, which is shown in Fig. 11b by the black marker. The distance on the Poincaré section between the reachable set and the stable manifolds is defined as the function d,

$$d(\boldsymbol{x}(N)) = \sqrt{(x - x_t)^2 + (\dot{x} - \dot{x}_t)^2}.$$

From the reachable set, the trajectory which minimizes d is used to initialize the next iteration. The minimum trajectory is also shown in Fig. 11a and is used to initialize the following stage. Over the relatively short time horizon of the geostationary orbital period, the reachability set remains quite close to the initial orbit. However, the addition of the control input has increased the velocity component of the trajectory. It is this velocity change that is subsequently exploited to generate the transfer trajectory.

The minimum trajectory from the first iteration of the reachability set is used to initialize the following stage. From the terminal state of the first iteration, the second reachability set is computed and displayed in Fig. 11c and d. The second reachability set is shown on the Poincaré section in Fig. 11d. This iteration greatly decreases the distance in the x component between the trajectory and the target, at the expense of a small deviation in the $\dot{x}$ component. In Fig. 11c, the first stage trajectory is shown in red while the additional stage is shown in blue, which demonstrates the decrease in the x component.

With each reachable set we move the controlled trajectory closer to the target stable manifold. Figures 11 and 12 shows all of the intermediate reachability iterations to transfer between the initial orbit and the stable invariant manifold. The final reachable set intersects the stable manifold of the periodic orbit. A final fixed terminal time and terminal state optimal transfer is finally used to arrive at the stable manifold.
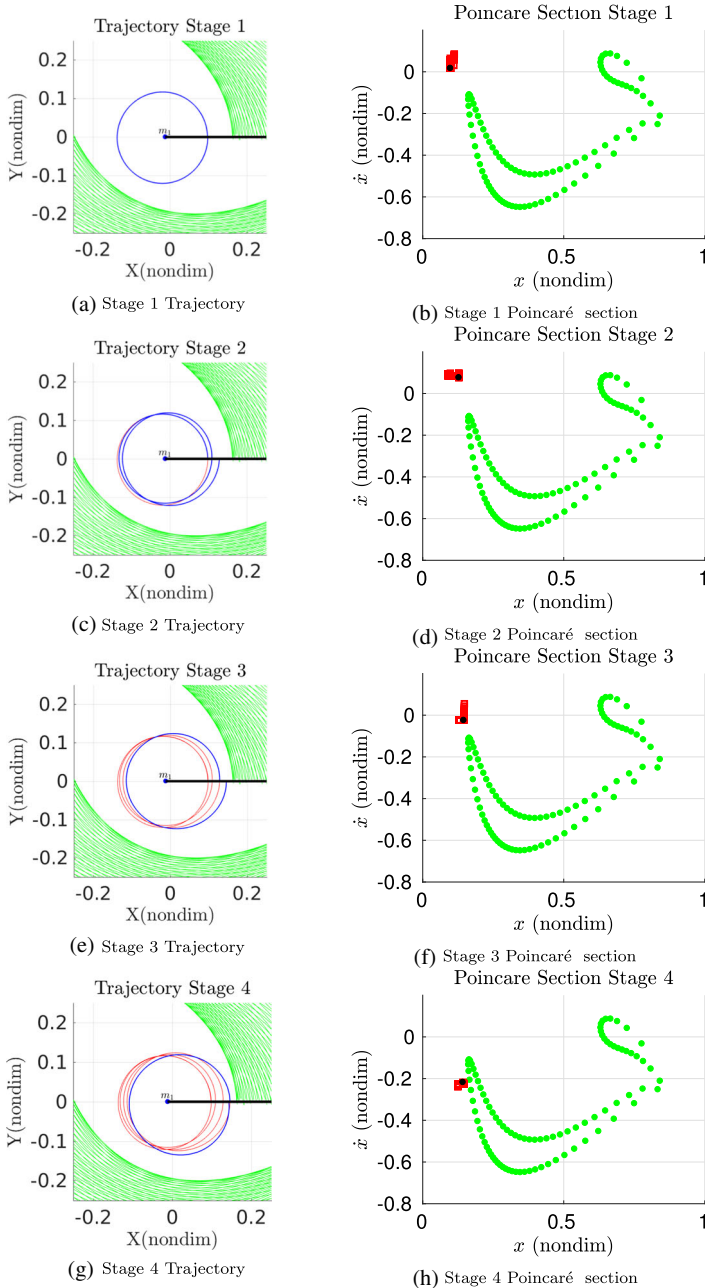
(a) Stage 1 Trajectory

(b) Stage 1 Poincaré section

(c) Stage 2 Trajectory

(d) Stage 2 Poincaré section

(e) Stage 3 Trajectory

(f) Stage 3 Poincaré section

(g) Stage 4 Trajectory

(h) Stage 4 Poincaré section

Fig. 11 Stage 1-4 reachability sets: The first four reachability sets visualized in both the position (left) and Poincaré space (right). The minimum trajectories from the preceding stages are shown in red, while the next stage is shown in blue. The transfer goal is to generate a complete trajectory from the initial geostationary orbit to the L_1 stable manifold, with an eventual arrival at the L_1 periodic orbit

(a) Stage 5 Trajectory

(b) Stage 5 Poincaré section

(c) Stage 6 Trajectory

(d) Stage 6 Poincaré section

(e) Stage 7 Trajectory

(f) Stage 7 Poincaré section

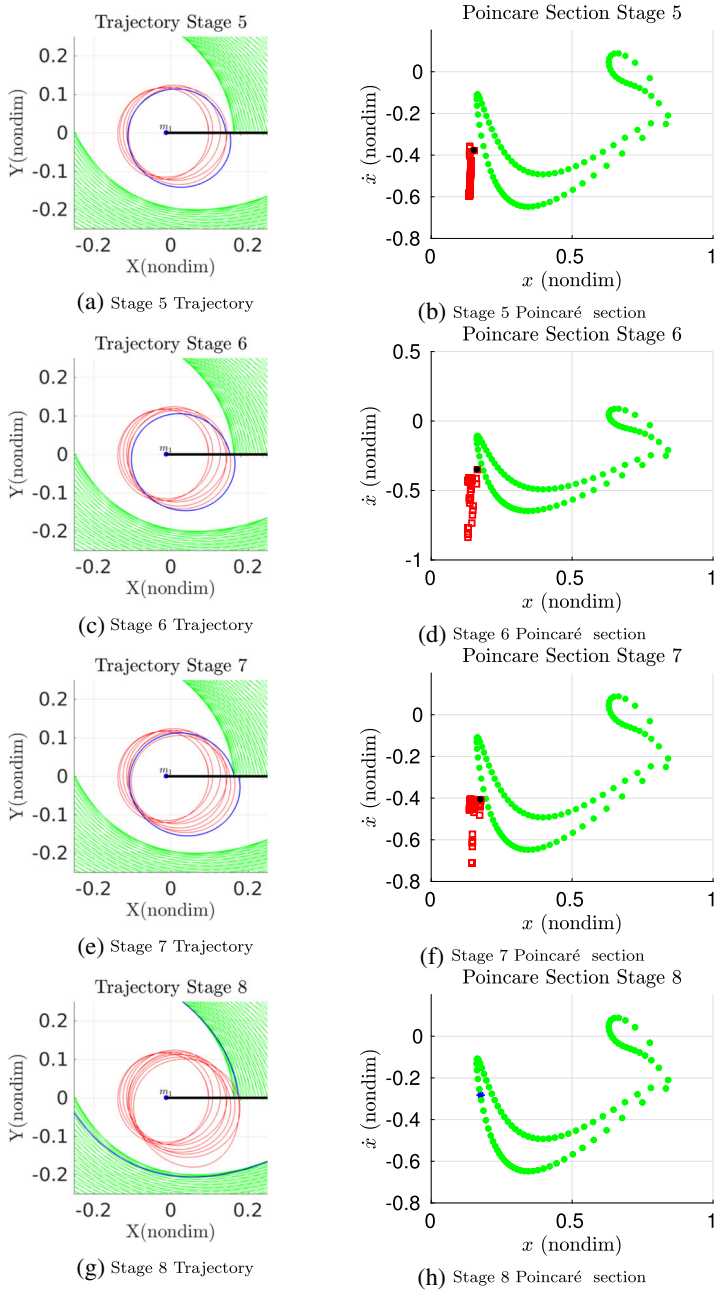(g) Stage 8 Trajectory

(h) Stage 8 Poincaré section

Fig. 12 Stage 5-8 reachability sets: The last four reachability sets visualized in both the position (left) and Poincaré space (right). The minimum trajectories from the preceding stages are shown in red, while the next stage is shown in blue. The transfer goal is to generate a complete trajectory from the initial geostationary orbit to the L_1 stable manifold, with an eventual arrival at the L_1 periodic orbit

(a) Transfer trajectory: Complete trajectory consisting of eight iterations (1-7 black and final in red) of the reachability sets with a final control-free coast (blue) on the stable manifold (green).

(b) Detailed view of transfer: Centered at m_1 the eight iterations from the reachability analysis are shown in black. The final segment to the stable manifold is shown in red. Each iteration progressively approaches the stable manifold. Once on the stable manifold the vehicle can coast without thrust towards the periodic orbit.

(c) Poincaré section: Minimum distance states from each iteration of the reachability set analysis (red) with respect to the stable invariant manifold (green)

(d) Control Input: Combined control history for each stage of the reachability analysis. The control always remains within the maximum bound.

(e) Jacobi Energy: Energy history throughout the transfer. Each stage of the transfer serves to increase the energy towards the stable manifold. The final reachability set intersects the stable manifold and enables a large final maneuver to the target orbit.
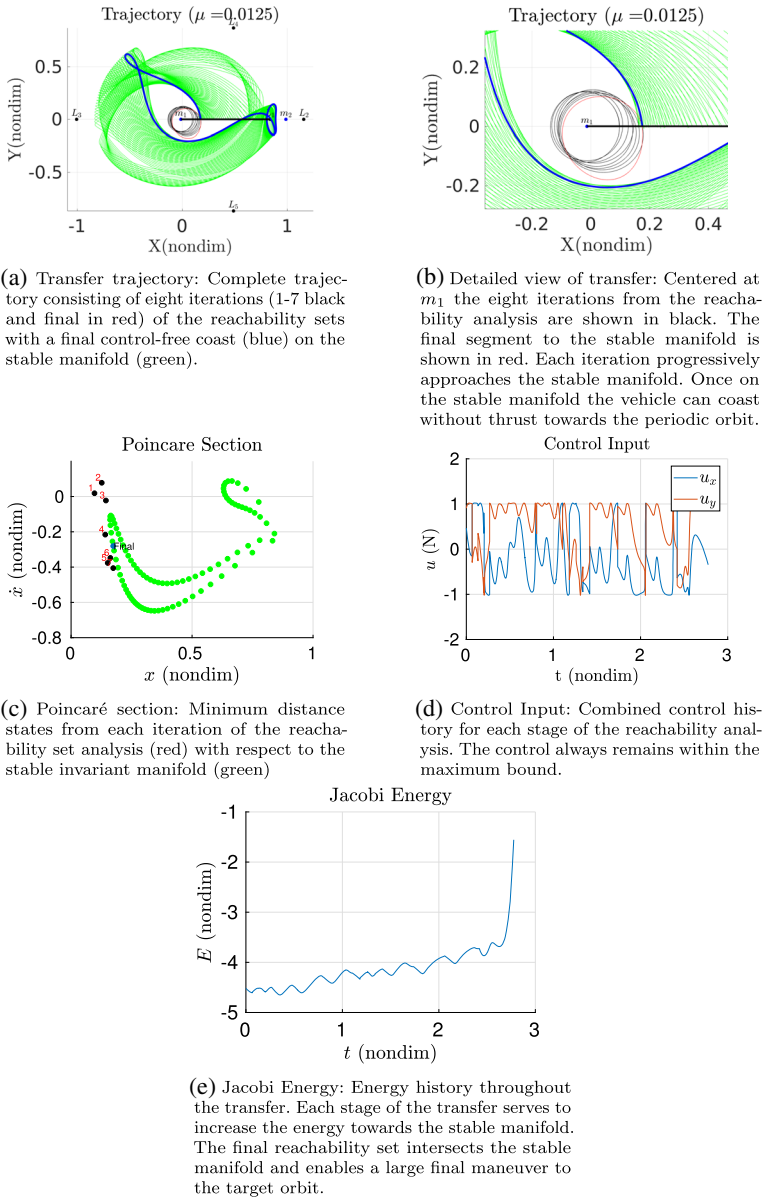
Fig. 13 Geostationary to L_1 periodic orbit transfer: Complete transfer from the geostationary orbit to the stable manifold

The optimization statistics for the final transfer are shown in Table 3. The complete transfer trajectory, after eight iterations, is shown in Fig. 13. Combining these trajectories results in the powered portion of the transfer from the geostationary orbit to the stable manifold. Each iteration systematically moves the reachable set towards

Table 3 Convergence statistics for the geostationary orbit transfer

Metric	Value
`fsolve` objective	1.42×10^{-11}
`fsolve` major iterations	18
`fsolve` first order optimality	7.2×10^{-11}
Optimal cost	4.30×10^{-25}
Execution time	2.62 s

the stable manifold. Furthermore, the optimal control formulation is simplified as each iteration is initialized using a simple distance metric on the Poincaré section. Figure 13a and b shows the resulting trajectory, with the final trajectory shown in red which ensures the intersection with the stable invariant manifold. Figure 13c shows the Poincaré section with the minimum reachable state from each iteration. Each iteration seeks to decrease the distance to the stable manifold on the Poincaré section. Furthermore, these minimum states serve to initialize each subsequent stage of the transfer. This method provides a systematic and simple methodology to determine transfer trajectories. Instead of relying purely on numerical optimization to find an appropriate trajectory, our method instead utilizes the reachability set to determine suitable trajectories. Once at the stable manifold, no further control input is required and the vehicle will coast towards the target periodic orbit. Figure 13d shows the control input during the powered portion of the transfer. We utilize the same spacecraft assumption of 500 kg from Section "Periodic Orbit transfer" which gives a maximum thrust of approximately 1 N. The spacecraft maintains a bounded control magnitude during the transfer to the stable manifold. Figure 13e shows the evolution of the Jacobi energy over the transfer. Each stage of the transfer serves to raise the energy level of the vehicle. After eight stages the reachability set intersects the stable manifold and a demonstrates that a transfer is achievable. The final optimal control drives the vehicle towards the target manifold with the appropriate energy level.

This numerical example demonstrates the ability to link several computations of the reachability set to enable a more general transfer. We use eight iterations of computing the reachability set in order to transfer from the geostationary orbit to the stable manifold. The example shows a transfer between an initial geostationary orbit and the stable manifold associated with a periodic orbit. This approach allows for a larger class of potential transfers which leverage the capabilities of low-thrust propulsion systems. However, the presented approach does not offer a optimal solution in terms of energy/fuel usage. The reachability sets are computed on the lower dimensional Poincaré section. As a result, the repeated intersections of the trajectory with the Poincaré section results in a fuel inefficient transfer. Furthermore, the issue of discrepancy in the Jacobi integral may become more serious when multiple reachability sets are interconnected. Nonetheless, we are able to apply the proposed approach for the challenging case where the reachability set is not sufficiently close to the invariant manifold of the target orbit. Consequently, this example illustrates a straightforward method to depart from the natural dynamics

and transfer to a large region of the phase space that is not accessible via invariant manifolds alone. The presented idea of connecting reachability sets can be further studied to address the aforementioned issues of optimality and mismatch of the Jacobi integral.

Conclusions

In this paper, we construct a systematic approach which combines the concepts of reachability sets and Poincaré sections to generate orbital transfers between planar periodic orbits in the three-body problem using low-thrust propulsion systems. The Poincaré section allows for trajectory design on a lower dimensional phase space thereby reducing the complexity and search space. The approximation of the reachability set enables a simple methodology for the selection of *good* initial parameters which will allow for convergence of the optimal control formulation. The combination of these two concepts allows the engineer to capture the characteristics inherent in the three-body problem. Additionally, we utilize geometric integrators to efficiently capture the long-term effects of low-thrust on the system dynamics. Our approach enables the computation of orbital transfers within the three-body problem but does not guarantee optimality of the resulting transfer. Instead, the resulting transfers will require no excessive control inputs as it is formulated as a deviation from the control-free trajectory. The presented approach allows for a systematic method to determine and generate orbital transfers in the three-body problem using low-thrust propulsion.

There is additional research to extend these results to more general transfer scenarios in future work. The incorporation of fourth body perturbations, such as the Sun in the Earth-Moon system, offers an additional method of increasing the reachable set with the combined use of the solar perturbation and low-thrust propulsion. In addition, the assumed acceleration magnitude is currently beyond the capabilities of current electric propulsion systems and future research is aimed at investigating smaller magnitude control inputs. Furthermore, this analysis did not consider the effect of variable mass on the optimal control solution. This will result in a more complicated optimal control problem and is a focus of future research. Finally, Lyapunov control theory, which has previously been applied to the two-body problem, is being investigated in the hope of designing closed loop control schemes for this three-body scenario [2]. The addition of attitude dynamics and realistic pointing constraints would also significantly improve the applicability of this work.

Appendix: Costate Equations of Motion

The development of the costate equations of motions begins with determining the second order partial derivatives of the gravitational potential. Due to the symmetry of partial derivatives only three terms are required and are given by

$$U_{xx_k} = (1 - \mu) \left[\frac{1}{r_{1_k}^3} - \frac{3(x_k + \mu)^2}{r_{1_k}^5} \right] + \mu \left[\frac{1}{r_{2_k}^3} - \frac{3(x_k - 1 + \mu)^2}{r_{2_k}^5} \right], \quad (20)$$

$$U_{yy_k} = (1 - \mu) \left[\frac{1}{r_{1_k}^3} - \frac{3y_k^2}{r_{1_k}^5} \right] + \mu \left[\frac{1}{r_{2_k}^3} - \frac{3y_k^2}{r_{2_k}^5} \right], \quad (21)$$

$$U_{xy_k} = U_{yx_k} = \frac{-3(1 - \mu)(x_k + \mu)y_k}{r_{1_k}^3} - \frac{3\mu y_k(x_k - 1 + \mu)}{r_{2_k}^5}. \quad (22)$$

The gradient of Eq. 10a is given as

$$f_{1_x} = \frac{1}{1 + h^2} \left[h^2 + 1 + \frac{h^2}{2} - \frac{h^3}{2} U_{yx_k} - \frac{h^2}{2} U_{xx_k} \right], \quad (23a)$$

$$f_{1_y} = \frac{1}{1 + h^2} \left[\frac{h^3}{2} - \frac{h^3}{2} U_{yy_k} - \frac{h^2}{2} U_{xy_k} \right], \quad (23b)$$

$$f_{1_{\dot{x}}} = \frac{h}{1 + h^2}, \quad (23c)$$

$$f_{1_{\dot{y}}} = \frac{h^2}{1 + h^2}. \quad (23d)$$

The gradient of Eq. 10b is given as

$$f_{2_x} = h - h f_{1_x} - \frac{h^2}{2} U_{yx_k}, \quad (24a)$$

$$f_{2_y} = -h f_{1_y} + 1 + \frac{h^2}{2} - \frac{h^2}{2} U_{yy_k}, \quad (24b)$$

$$f_{2_{\dot{x}}} = -h f_{1_{\dot{x}}}, \quad (24c)$$

$$f_{2_{\dot{y}}} = h - h f_{1_{\dot{y}}}. \quad (24d)$$

The gradients of Eqs. 12c and 12d are given as

$$\frac{\partial r_{1_k} p}{\partial \bar{x}} = \left((x_{k+1} + \mu)^2 + y_k p^2 \right)^{-\frac{1}{2}} \left[(x_{k+1} + \mu) f_{1_{\bar{x}}} + y_k p f_{2_{\bar{x}}} \right], \quad (25a)$$

$$\frac{\partial r_{2_k} p}{\partial \bar{x}} = \left((x_{k+1} - 1 + \mu)^2 + y_k p^2 \right)^{-\frac{1}{2}} \left[(x_{k+1} - 1 + \mu) f_{1_{\bar{x}}} + y_k p f_{2_{\bar{x}}} \right]. \quad (25b)$$

The second order partial derivatives of the gravitational potential at $k+1$ are given as

$$\frac{\partial U_{xx_{k+1}}}{\partial \bar{x}} = (1-\mu)\left[\frac{1}{r_{1_k}p^3}f_{1_{\bar{x}}} - \frac{3\,(x_{k+1}+mu)}{r_{1_k}p^4}\frac{\partial r_{1_k}p}{\partial \bar{x}}\right]$$

$$+\mu\left[\frac{1}{r_{2_k}p^3}f_{1_{\bar{x}}} - \frac{-3\,(x_{k+1}-1+\mu)}{r_{2_k}p^4}\frac{\partial r_{2_k}p}{\partial \bar{x}}\right], \tag{26a}$$

$$\frac{\partial U_{yx_{k+1}}}{\partial \bar{x}} = (1-\mu)\left[\frac{1}{r_{1_k}p^3}f_{2_{\bar{x}}} - \frac{3y_k p}{r_{1_k}p^4}\frac{\partial r_{1_k}p}{\partial \bar{x}}\right]$$

$$+\mu\left[\frac{1}{r_{2_k}p^3}f_{2_{\bar{x}}} - \frac{-3y_k p}{r_{2_k}p^4}\frac{\partial r_{2_k}p}{\partial \bar{x}}\right]. \tag{26b}$$

The gradient of Eqs. 10c and 10d are given as

$$f_{3_x} = 2f_{2_x} + \frac{h}{2}\left(f_{1_x}+1\right) - \frac{h}{2}U_{xx_{k+1}} - \frac{h}{2}U_{xx_k}, \tag{27a}$$

$$f_{3_y} = -2 + 2f_{2_y} + \frac{h}{2}f_{1_y} - \frac{h}{2}U_{xy_k p} - \frac{h}{2}U_{xy_k}, \tag{27b}$$

$$f_{3_{\dot{x}}} = 1 + 2f_{2_{\dot{x}}} + \frac{h}{2}f_{1_{\dot{x}}} - \frac{h}{2}U_{x\dot{x}_{k+1}}, \tag{27c}$$

$$f_{3_{\dot{y}}} = 2f_{2_{\dot{y}}}, \tag{27d}$$

$$f_{4_x} = 2 - 2f_{1_x} + \frac{h}{2}f_{2_x} - \frac{h}{2}U_{yx_{k+1}} - \frac{h}{2}U_{yx_k}, \tag{28a}$$

$$f_{4_y} = -2f_{1_y} - \frac{h}{2}\left(f_{2_y}+1\right) - \frac{h}{2}U_{yy_k p} - \frac{h}{2}U_{yy_k}, \tag{28b}$$

$$f_{4_{\dot{x}}} = -2f_{1_{\dot{x}}} + \frac{h}{2}f_{2_{\dot{x}}} - \frac{h}{2}U_{y\dot{x}_{k+1}}, \tag{28c}$$

$$f_{4_{\dot{y}}} = 1 - 2f_{1_{\dot{y}}} + \frac{h}{2}f_{2_{\dot{y}}} - \frac{h}{2}U_{y\dot{y}_{k+1}}. \tag{28d}$$

These gradient equations are in a cascade type structure. Equations 27a–d and 28a–d are functions of Eqs. 10c and 10d. As a result, the accuracy of the Jacobian will tend to decrease as the first order approximation errors accumulate.

References

1. Bryson, A.E., Ho, Y.C.: Applied Optimal Control: Optimization, Estimation and Control. CRC Press (1975)
2. Chang, D.E., Chichka, D.F., Marsden, J.E.: Lyapunov-based transfer between elliptic Keplerian orbits. Discret. Cont. Dyn. Syst. Series B **2**(1), 57–68 (2002)
3. Choueiri, E.Y.: New dawn for electric rockets. Sci. Am. **300**(2), 58–65 (2009). https://doi.org/10.1038/scientificamerican0209-58
4. Conley, C.C.: Low energy transit orbits in the restricted three-body problem. SIAM J. Appl. Math. **16**(4), 732–746 (1968). http://www.jstor.org/stable/2099124

5. Dellnitz, M., Junge, O., Post, M., Thiere, B.: On target for venus – set oriented computation of energy efficient low thrust trajectories. Celest. Mech. Dyn. Astron. **95**(1-4), 357–370 (2006). https://doi.org/10.1007/s10569-006-9008-y

6. Folta, D., Dichmann, D., Clark, P., Haapala, A., Howell, K.: Lunar cube transfer trajectory options. In: Proceedings of the AAS/AIAA Spaceflight Mechanics Meeting, p. 353. Williamsburg (2015)

7. Gómez, G., Koon, W., Lo, M.W., Marsden, J., Masdemont, J., Ross, S.: Invariant manifolds, the spatial three-body problem and space mission design. In: AAS/AIAA Astrodynamics Specialist Conference. American Astronautical Society, Quebec City (2001)

8. Grebow, D.J., Ozimek, M.T., Howell, K.C.: Design of optimal low-thrust lunar pole-sitter missions. J. Astronaut. Sci. **58**(1), 55–79 (2011). https://doi.org/10.1007/BF03321159

9. Haque, S.E., Keidar, M., Lee, T.: Low-thrust orbital maneuver analysis for cubesat spacecraft with a micro-cathode arc thruster subsystem. In: Proceedings of the Thirty-Third International Electric Propulsion Conference. Electric Rocket Propulsion Society, Washington DC (2013)

10. Holzinger, M., Scheeres, D.: Reachability analysis applied to space situational awareness. In: Advanced Maui Optical and Space Surveillance Technologies Conference (2009)

11. Kirk, D.E.: Optimal Control Theory: An Introduction. Courier Corporation (2012)

12. Komendera, E.E., Scheeres, D.J., Bradley, E.: Intelligent computation of reachability sets for space missions. In: IAAI (2012)

13. Koon, W.S., Lo, M.W., Marsden, J.E., Ross, S.D.: Heteroclinic connections between periodic orbits and resonance transitions in celestial mechanics. Chaos: Interdiscip. J. Nonlinear Sci. **10**(2), 427–469 (2000)

14. Koon, W.S., Lo, M.W., Marsden, J.E., Ross, S.D.: Dynamical systems, the three-body problem and space mission design. Marsden Books. http://www2.esm.vt.edu/~sdross/books/ (2011)

15. Kulumani, S., Lee, T.: Low-thrust trajectory design using reachability sets near asteroid 4769 castalia. In: Proceedings of the AIAA / AAS Astrodynamics Specialists Conference. Long Beach. https://doi.org/10.2514/6.2016-5376 (2016)

16. Lanczos, C.: The Variational Principles of Mechanics, vol. 4. Courier Corporation (1970)

17. Llibre, J., Martínez, R., Simó, C.: Tranversality of the invariant manifolds associated to the Lyapunov family of periodic orbits near l_2 in the restricted three-body problem. J. Diff. Equ. **58**(1), 104–156 (1985). https://doi.org/10.1016/0022-0396(85)90024-5. http://www.sciencedirect.com/science/article/pii/0022039685900245

18. Lo, M.W.: Libration point trajectory. Design **14**(1–3), 153–164 (1997). https://doi.org/10.1023/A:1019108929089

19. Lygeros, J.: On the relation of reachability to minimum cost optimal control. In: Proceedings of the 41st IEEE Conference on Decision and Control, 2002, vol. 2, pp. 1910–1915. https://doi.org/10.1109/CDC.2002.1184805 (2002)

20. Lygeros, J.: On reachability and minimum cost optimal control. Automatica **40**(6), 917–927 (2004). https://doi.org/10.1016/j.automatica.2004.01.012. http://www.sciencedirect.com/science/article/pii/S0005109804000263

21. Marsden, J.E., West, M.: Discrete mechanics and variational integrators. Acta Numerica **2001**(10), 357–514 (2001)

22. Mingotti, G., Topputo, F., Bernelli-Zazzera, F.: Earth–mars transfers with ballistic escape and low-thrust capture. Celest. Mech. Dyn. Astron. **110**(2), 169–188 (2011). https://doi.org/10.1007/s10569-011-9343-5

23. Ozimek, M.T., Howell, K.C.: Low-thrust transfers in the earth-moon system, including applications to libration point orbits. J. Guid. Control Dyn. **33**(2), 533–549 (2010). https://doi.org/10.2514/1.43179

24. Pellegrini, E., Russell, R.P.: On the computation and accuracy of trajectory state transition matrices. J. Guid. Control Dyn., 39. https://doi.org/10.2514/1.G001920 (2016)

25. Ross, S.D.: The interplanetary transport network. Am. Scient. **94**(3), 230 (2006)

26. Schmidt, G.R., Patterson, M.J., Benson, S.W.: The nasa evolutionary xenon thruster (next): The next step for us deep space propulsion. NASA Glenn Research Center. Document IAC-08-C4, vol. 4 (2008)

27. Stoer, J., Bulirsch, R.: Introduction to Numerical Analysis, Texts in Applied Mathematics, vol. 12. Springer, New York (2013)

28. Szebehely, V.: Theory of Orbits. The Restricted Problem of Three Bodies, p. 1. Academic Press, New York (1967)

29. Varaiya, P.: Reach set computation using optimal control. In: Verification of Digital and Hybrid Systems, pp. 323–331. Springer (2000)

30. West, M.: Variational integrators. Ph.D. thesis, California Institute of Technology (2004)